Reactive and Functional Polymers

CO_2 adsorption capacities of amine-functionalized microporous silica nanoparticles

Eduardo J. Cueto-Díaz,[a*] Fabián Suárez-García,[b] Santos Gálvez-Martínez,[a] María Pilar Valles González,[c] Eva Mateo-Marti.[a]

[a] Centro de Astrobiología (CSIC-INTA), Ctra. Ajalvir, Km.4, 28850, Torrejón de Ardoz, Madrid, Spain.

[b] Instituto de Ciencia y Tecnología del Carbono, INCAR-CSIC. C/ Francisco Pintado Fe, 26, 33011, Oviedo, Spain.

[c] Instituto Nacional de Técnica Aeroespacial (INTA), Departamento de Materiales y Estructuras. Ctra. Ajalvir, Km.4, 28850, Torrejón de Ardoz, Madrid, Spain.

[*] E-mail: ecueto@cab.inta-csic.es

TOC graphic

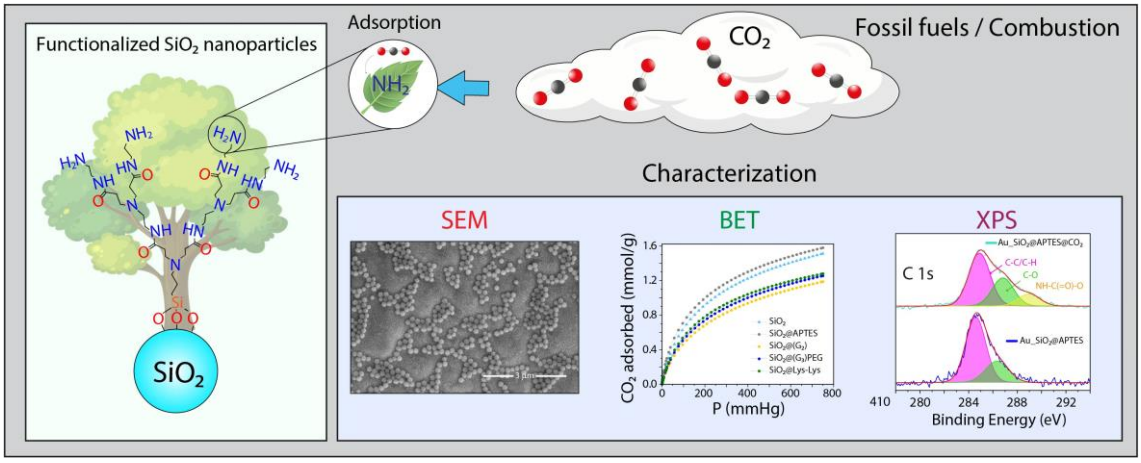

ABSTRACT

Efforts on CO_2 capture have intensified as climate change compromises ecosystems and biodiversity. Therefore, it is crucial to develop different methods for CO_2 sequestration to improve solid sorbent capabilities (NPs). To this end, the surface of 200-nm silica nanoparticles (SiO_2NPs) was covalently anchored with aminated ligands, 3-aminopropyltriethoxysilane (APTES), poly(amidoamine) dendrimers (PAMAM) and a short peptide comprising two lysine units, aiming for CO_2 adsorption over a wide range of pressures. Our goal was to explore the influence of functional chemical groups (attached to the SiO_2NPs) on CO_2 sequestration. The observed results showed that at low and high CO_2 gas pressure conditions, typical APTES-functionalized SiO_2Np surpassed the CO_2 adsorption capacities of dendritic and peptide-based nanoparticles bearing amine-polymer functionalities, a remarkable effect that was investigated in this work. In addition, a convenient and facile method to decorate and quantify SiO_2 nanoparticles with PAMAM and a short peptide is reported.

KEYWORDS. Hybrid silica nanoparticles, CO_2 isotherms

Highlights

- Functionalization of SiO_2 nanoparticles with a self-synthesized Lys-Lys peptide was conducted. Peptide loading was also quantified by a second colorimetric analysis protocol.
- CO_2 adsorption capacities of hybrid and “naked” nanoparticles were determined.
- Spectroscopic and microscopic characterization of the aminosilane ligand-SiO_2NP systems was conducted.
- The amine loading and textural properties of the nanomaterials were studied.

1. INTRODUCTION

Postcombustion CO_2 capture (PCC) is currently one of the most developed and implemented technologies for CO_2 retention. PCC involves the removal of CO_2 from flue gases after combustion of fossil fuels, such as coal, crude oil, and natural gas, typically followed by a desorption route enabling an overall cyclic process. There are many post-combustion capture technologies, such as Ca-Looping technology [1], membrane separation [2], cryogenic fractionation [3], and adsorption[4]. However, the most employed tool involves passing the CO_2 flue gas through a solvent, commonly monoethanolamine (MEA), in an adsorption column, followed by desorption or stripping. Overall, the major drawback to the application of post-combustion technologies is the low partial pressure of CO_2 in the flue gas at atmospheric pressure and concentration values that range from 13-15% [5]. This problem can be circumvented by the development of materials bearing large CO_2 adsorption capacities. In recent years, materials, such as MOFs [6], zeolites [7], silica [8], clay [9], activated carbons [10], and the previously mentioned MEA, have been extensively studied.

In this regard, amines, and concretely, primary amines, are well known for their reversible reactions with CO_2 [11], in particular monoethanolamine [12] (MEA), which has been implemented for PCC and recovery technology in recent years. However, despite its high absorption rate and relatively low cost, its use among other aqueous amine solutions [13] has several drawbacks, such as high corrosivity, low resistance to thermal and oxidative degradation, and the regeneration of MEA after CO_2 adsorption is also a direct source of this gas [12, 14]. Alternative amines and mixtures, such as piperazine/2-aminomethylpropanol (PZ/AMP) and methyl diethanolamine (MDEA), which maximize amine scrubbing, still face the high energy demand of heating the solution for solvent regeneration. Some of the new approaches [15-17] are devoted to avoiding these problems by their adsorption onto solid materials in which there is no bulk water that requires heating and lower regeneration energy is demanded. Thus, amine-modified solid sorbents combine the thermal and textural properties of porous materials with the high affinity of amines towards CO_2. Studies on this subject have been reported, i.e., Polshettiwar *et al.* [18, 19] and Jones *et al.* [20-24] screened amine-functionalized polymeric silica nanoparticles/MOFs, demonstrating the potential application of impregnated or covalently decorated nanomaterials with amine-based ligands for CO_2 capture. Therefore, driven by our preliminary studies [8] in which similar bare silica nanoparticle (SiO_2NP)

hosts exhibited good CO_2 sensing and fair adsorption features, we analysed the effect on the CO_2 capacity of bulky vs. nonbulky ligands covalently grafted on microporous nanospheres. We have therefore investigated a series of Class 2 sorbents by covalently incorporating i) 3-aminopropyltrimethoxysilane (APTES), ii) G_2 and G_3 PAMAM dendrons and iii) Lys-Lys into silica nanoparticle hosts (Figure 1) in a combined convergent/divergent approach.

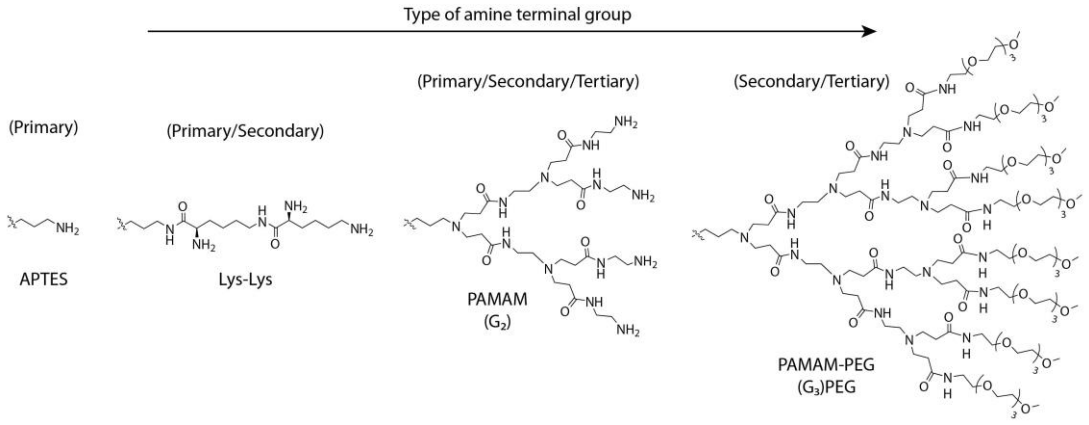

Figure 1. Schematic illustration of the different aminosilane ligands used in this study

The selection of these groups was not arbitrary, as APTES is recognized for enhancing CO_2 retention at high pressures [25]. A marked increase will be expected by using PAMAM dendrons due to the large number of structural amines supplied as well as the presence of internal cavities, thus favouring physisorption processes; additionally, a Lys-Lys peptide was studied from a prebiotic chemistry point of view. In summary, we present the CO_2 adsorption isotherms of a series of amine-functionalized silicas and their versatile synthesis processes. We also wanted to investigate the effect of biological entities that adhered onto silica frameworks in CO_2 adsorption processes. These studies at very low CO_2 pressures (7 mbar), in particular mimicking Martian atmospheric conditions, were performed inside a planetary atmosphere and surface simulation chamber (PASC, Figure S1) [26]. This study is also devoted to understanding the role of short peptides and amide/amine-based ligands covalently anchored in silica, which could have inhabited a primitive Earth or Mars, a CO_2-rich atmospheric planet. Furthermore, CO_2 adsorption from Mars' atmosphere on the regolith surface of the planet could have relevant implications for future planetary exploration.

2. MATERIALS AND METHODS

Detailed experimental procedures for the synthesis of Compounds **1-2**, as well as functionalized SiO_2 **(Scheme 1)** and their corresponding quantification analysis, are provided in the Supporting Information (ESI).

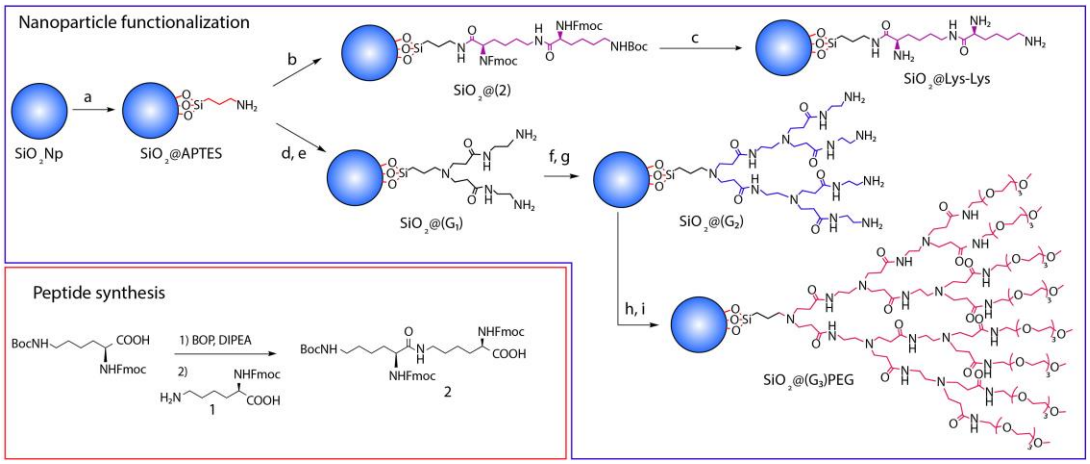

Scheme 1: (a) APTES, PhMe, 50 °C, 20 h (b) PyBOP, DIPEA, **2**, DMF, r.t., 18 h; (c) piperidine/DMF (1:3), r.t., 30 min, then DCM/TFA (2:1); (d) Methyl acrylate, EtOH, 40 °C, 5 h; (e) ethylenediamine, EtOH, 45 °C, 5 h; (f) methyl acrylate, EtOH, 40 °C, 5 h; (g) ethylenediamine, EtOH, 45 °C, 5 h (**5b**); (h) methyl acrylate, EtOH, 40 °C, 24 h; (i) NH_2-PEG, EtOH, 40 °C, 48 h

2.1. Chemical reagents

SiO_2Np (Nanocym), trifluoroacetic acid (TFA) 99%, (benzotriazol-1-yloxy)tris(dimethylamino)phosphonium hexafluorophosphate (BOP) 97%, *N*,*N*-diisopropylethylamine (DIPEA) >99%, dimethyl sulfoxide-d6 (DMSO-d_6), (3-mercaptopropyl)trimethoxysilane (MPTMS) >96%, *N*,*N*-dimethylformamide (DMF) 99.8%, dichloromethane anhydrous (DCM) 99%, 3-aminepropyltriethoxysilane (APTES) 98% and 3,6,9,12-tetraoxatridecanamine 98% were purchased from TCI Europe; Fmoc-L-Lys(Boc)-OH (Iris Biotech), ninhydrin 99% (Fisher), piperidine 99%, HPLC toluene, and hexylamine 99% were purchased from Sigma-Aldrich; HPLC methanol, ethylenediamine 99%, and methyl acrylate 98% were purchased from Merck.

2.2. Surface characterization

The surface chemistry and morphology of the nanoparticles were characterized by using different techniques:

X-ray photoelectron spectroscopy (XPS), Fourier transform infrared spectroscopy (FTIR), and scanning electron microscopy (SEM) (ESI for further details). In addition, particle size distribution and thermogravimetric analysis were performed.

2.3. N_2 and CO_2 adsorption capacities

The gas adsorption capacities of the samples were determined by measuring their N_2 adsorption-desorption isotherms at -196, 25 and 50°C, whereas CO_2 adsorption-desorption isotherms were recorded at 0, 25 and 50°C in an Autosorb-1 volumetric device (Quantachrome) in a 10^{-5} to 1 bat pressure range.

The selectivity of the adsorption of CO_2 over N_2 in a binary mixture of both gases at 25 and 50 °C was estimated from the individual adsorption isotherms of each gas at those temperatures, following the procedure explained in the ESI.

Finally, the cyclability and stability of these materials were determined for the selected samples by measuring five correlative CO_2 adsorption and desorption isotherms at 25 °C without any degasification step between the measurements.

2.4. Synthesis of the hybrid nanoparticles

The synthesis of the hybrid nanoparticles (Scheme 1 and Figures S2 to S8) was performed by adapting two methodologies [27, 28], employing SiO_2@APTES as the starting branching point, which was prepared using a protocol adapted from Chaix *et al.* [29]. Then, in a controlled multistep divergent synthesis, i) methyl acrylate (Michael addition) followed by ii) ethylenediamine condensation was performed. The sequence (Scheme 1d-g) was repeated, reaching a generation 2 PAMAM dendron leading to SiO_2@(G_2). The efficiency of the first- and second-generation steps was quantified using the ninhydrin test (ESI). Lastly (Scheme 1 h-j), in an effort to enhance the CO_2 adsorption capacities of SiO_2@(G_2), generation 3 was reached, and PEG-3 was connected to the periphery. This is expected to promote the retention of CO_2 inside the internal voids. Hence, methyl acrylate addition was followed by NH_2-PEG_3-OMe incorporation at 45 °C for 5 days, leading to the fourth type of functionalized nanoparticle, SiO_2@(G_3)PEG.

2.5. Synthesis of peptide and further SiO_2 functionalization

Lys-Lys (Scheme 1, S13-S15) was prepared according to the typical synthetic procedure *via* a BOP coupling reagent. In the first step, the fully protected Fmoc-Lys(Boc)-OH amino acid (500 mg) was N-Boc deprotected using a large excess of TFA (3 mL), thus leading to **1** quantitatively. In a second step, Fmoc-Lys(Boc)-OH was treated with BOP and DIPEA to generate the reactive intermediate RCOOBt ester species, which was subsequently aminolyzed to amide (**2**) in the presence of stoichiometric amounts of **1** (for details, see ESI). The peptide was then covalently grafted onto the surface of the silanized SiO_2 nanoparticles (SiO_2@APTES) that were PyBOP mediated (Scheme 1b), and in a

second step (Scheme 1c), double Fmoc deprotection was performed, and the amount of grafted peptide (**1**) was quantified by Fmoc-piperidine adduct assay. Finally, (Scheme S15) Boc was cleaved to afford SiO_2@Lys-Lys.

2.6. Colorimetric assays

Two different colorimetric assays were conducted for the quantification of the species attached to SiO_2. First, i) the amounts of APTES and G1/G2 PAMAM were determined by using the Kaiser test [30] (Figures S17-18), where the absorbance of the chromophore resulting from the reaction between the primary amines and ninhydrine was recorded at different concentrations. Thus, a value of 69 μmol (APTES)/g SiO_2 or 12.3 mg (APTES)/g SiO_2 and 88% and 78% yields were obtained in the generation 1 and 2 PAMAM syntheses, respectively. Then, ii) the amount of peptide, Lys-Lys, was obtained by conducting a dibenzofulvene piperidine adduct assay, as the base-labile Fmoc group when cleavage forms the dibenzofulvene-piperidine chromophore (Figure S20) exhibiting a $\varepsilon_{290} = 6.09x10^{-3}$ L mol^{-1} cm^{-1} at $\lambda^{abs} = 290$ nm. Then, the amount of peptide attached could be quantified, leading to 17.4 μmol (Lys-Lys)/g SiO_2. The overall peptide functionalization efficiency was estimated to be 25%.

3. RESULTS AND DISCUSSION

3.1. Identification of CO_2 fingerprints at 7 mbar

The FTIR spectra of Au_SiO_2@APTES (Figure 2), Au_SiO_2@Lys-Lys (Fig. S21) and the hybrid species Au_SiO_2@(G_2) (Figure S22) and Au_SiO_2@(G_3)PEG (Figure S24) were recorded before (blue) and after (red) CO_2 exposure inside PASC. Remarkably, the IR spectra broadened when the samples were exposed to atmospheric pressure of 7 mbar of CO_2, which is consistent with the adsorption of gas in both materials. Interestingly, for the case of Au_SiO_2@APTES, it displayed a major difference before and after CO_2 exposure. Here, the most significant IR regions were 470 cm^{-1} due Si-O bonds [31], 1100 cm^{-1} attributed to Si-O-Si asymmetric stretching vibrations [32], 1300 cm^{-1} ascribed to $NCOO^-$ skeletal vibrations [33], and the bands located at 1650 cm^{-1} and 2900 cm^{-1} assigned to asymmetric and symmetric bending of the primary amine (NH_2) but are also in the range of CH and OH, respectively.

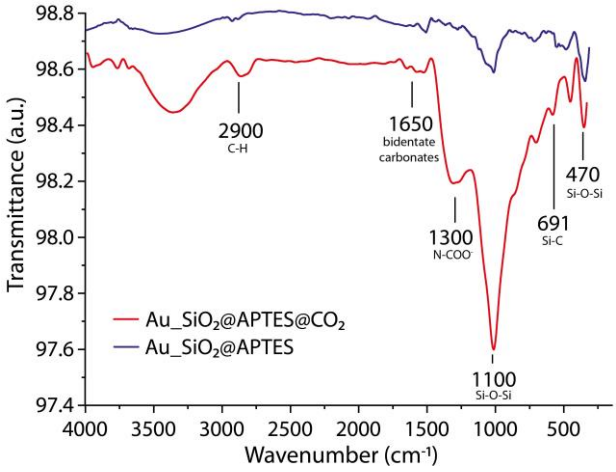

Figure 2. Superimposed IR spectra of Au_SiO_2@APTES and Au_SiO_2@APTES@CO_2

For the other nanoobjects of study, a few remarks need to be highlighted. When comparing Au_SiO_2@(G_2) vs. Au_SiO_2@(G_2)@CO_2 (before and after PASC), two main differences were noticeable: a) a broad peak emerged at 1865 cm^{-1} after CO_2 exposure inside PASC, which could be attributed to the C=O species (carbonate) formed between the PAMAM dendron and the CO_2 (R-CO-O-CO-R) (e.g., an anhydride functional group), and b) the vanishing peak at 1400 cm^{-1} might be ascribed to the chemical modification in the vicinity of the amides in the PAMAM dendrons. Finally, there was no marked difference between Au_SiO_2@(G_3)PEG and Au_SiO_2@(G_3)PEG@CO_2 or in the peptide (Lys-Lys) case; however, the IR spectra provided insight into the synthetic steps, confirming the success of the incorporation of PEG chains at the very last step of the synthesis of SiO_2@(G_3)PEG (peak at 2900 cm^{-1}, Figure S23 inset).[34] In addition, to confirm the presence of the different aminosilane ligands linked to the nanoparticles,

XPS analysis was performed in the four different samples: Au_SiO_2NP (described in our previous work[8]), Au_SiO_2@APTES, Au_SiO_2@Lys-Lys and Au_SiO_2@(G_3)PEG.

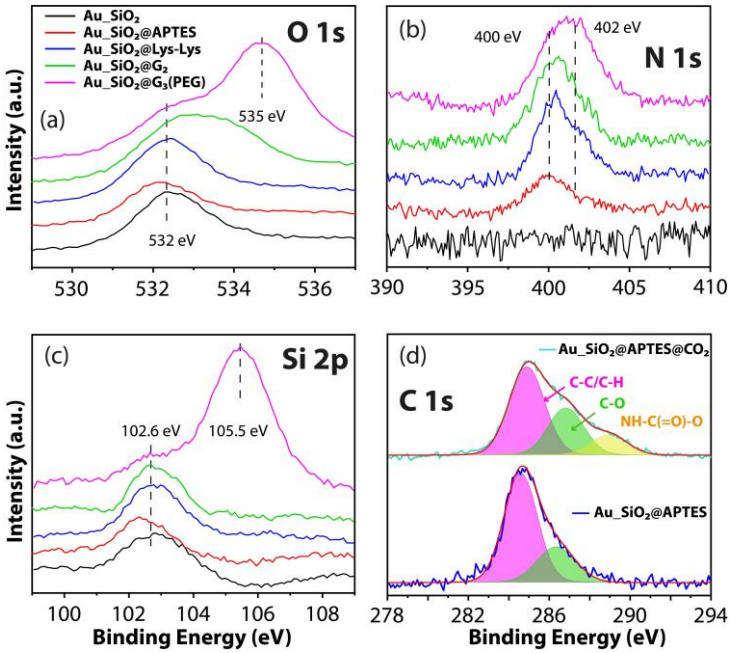

Figure 3. (a-c) XPS spectra of the nanoparticles immobilized over Au wafers in the regions of (a) O 1s, (b) N 1s and (c) Si 2p; and (d) XPS spectra of Au_SiO_2@APTES before and after CO_2 exposure in PASC, (C 1s)

The XPS spectra overview of the four different wafers shows that the following atomic species can be identified: O, C, Si and Au. Furthermore, the presence of nitrogen was identified for the aminosilane ligands, confirming the successful linkage to the Au-NPs. The intensity of the nitrogen signal is related to the amount of nitrogen present on the chemical structure, confirming their existence on the surface adsorption (wafers). The N1s peak shows two components at 399.9 eV and 401.9 eV, the first one assigned to the $NH_{2[35]}$ amide group (-NH-CO-) and tertiary amine (NR_3) and the second one assigned to NH_3^+ occurring even in slightly basic solutions with new bonds taking place between the G_3 (PEG) and the nanoparticles' surface, which is in good agreement with the chemical structure of the specific ligands (Figure 3a). Therefore, the signal enhancement of the second component is remarkable, which could be related to the appearance of new bonds taking place between G_3(PEG) and the nanoparticle surface in Au_SiO_2@(G_3)PEG (Figure 3a). Furthermore, to confirm the presence of chemisorbed CO_2, XPS analysis was performed for the same four samples after exposure to a CO_2 atmosphere inside the PASC chamber. There was no apparent change in any of the hybrid nanomaterials, except for

the APTES-functionalized nanoparticles. Figure 3b shows the XPS core-level spectra of C 1s in both cases (Au_SiO_2@APTES and Au_SiO_2@APTES@CO_2). The best-fit curve for the C 1s peak (SiO_2@APTES) was achieved using two components. The first carbon component has a binding energy (B.E.) of 284.6 eV and is attributed to the C-H and C-C groups, and the second component at 286.3 eV corresponds to O-CH_3 groups and C-N groups. Remarkably, the appearance of a third component at 289.0 eV, assigned to the carbamate (NH-C(=O)-O) groups when SiO_2@APTES was exposed to CO_2, supports the idea of APTES-functionalized silica nanoparticles as suitable materials for CO_2 adsorption at low pressures. This is in good agreement with the infrared analysis. Both complementary spectroscopies, XPS and infrared, helped us to identify the CO_2 adsorption process and chemical adsorption species, confirming the fingerprint signal when the CO_2 fixation process is preferential in the APTES case rather than for the other amino ligands (Lys-Lys and PEG). A carbon component comparison study of the samples before and after CO_2 exposure was performed, and the results are shown in Table S1. There was no marked increase in the component at 289.0 eV for either the Lys-Lys or PEG cases after CO_2 exposure, which was expected to occur due to the number of available nitrogen atoms in their chemical structure. This could be explained if the ligands collapse over the SiO_2, producing new bonds between the ligands and the NP surface and blocking the efficiency of CO_2 capture. Therefore, even if we were expecting that amino ligands bearing higher amounts of nitrogen in their chemical structure would give better CO_2 adsorption efficiency, our experiments showed that this is not the case (see Table S1). Table S1 shows a carbon component comparison study between samples before and after CO_2 exposure for the three different cases, and the percentage increase of the component was assigned to the process at ca. 289.0 eV. There was no increase in component 289.0 for either the Lys-Lys or PEG cases after CO_2 exposure. This is surprising as the amount of primary amine groups increased. For Lys-Lys, not all the nitrogen atoms are available, and for PEG, it seems that the structure collapses, producing new bonds between the O groups from the molecule and the silicon from the nanoparticle (O-Si) or even intramolecular interactions, which block the chemical structure, thus preventing the efficiency of CO_2 adsorption. Finally, Figures 3c and 3d show the core-level XPS spectra of the O 1s and Si 2p regions for the four studied cases before CO_2 exposure inside PASC. The Si 2p peak is observed at ~ 102.6 eV, which was ascribed to the linkage of SiO_2NPs into the gold wafer (Figure 3c), and the appearance of a new peak, in Au_SiO_2@G_3(PEG), shifted to 105.5 eV due to the presence of electron-withdrawing

groups in the surface, which may be a result of the collapse of the amide-base scaffolding towards the surface of the SiO_2Nps, diminishing their CO_2 adsorption capacity. This behaviour seems to fit with the potential formation of Si(CO_3^{2-}) species and Si(NO) [36, 37], even if the sensor was deprived of a CO_2 atmosphere; therefore, this initial blocking state of the reactive functional groups made the CO_2 adsorption process unable to proceed. In addition, the best-fit curves for the O 1 s, depicted in Figure 3d, displayed a similar trend as silicon, where there is only one component at 532.0 eV for the NP, APTES and Lys-Lys cases. The case of Au_SiO_2@(G_3)PEG shows two main components: one is observed at 531.7 eV, attributed to OH and Si-O species, and the second is, in accordance with the silicon case, at approximately 534.7 eV, which is related to interactions between the surface and the PEGylated dendritic scaffold (C-O, N-O) [38-40].

3.2. Morphology of the functionalized nanoparticles

The morphology of the nanomaterials, as well as the immobilization features, were investigated by scanning electron microscopy (SEM). As shown in Figure 4, the samples displayed regular and spherical morphology with a nanoparticle size of 199 ± 7 nm and predominant single-layer deposition. However, the samples coated with peptide and dendrons, as shown in Figures 4b and 4c-d, respectively, showed aggregation tendencies due to plausible interdigitation between the bulky peripheral layers. In addition to the SEM microscopy studies, particle size measurements (Figure 4, right) were conducted in the bare SiO_2NPs, and the data were compared; thus, the experimental values obtained with both techniques were in agreement, demonstrating that 200 nm is the average hydrodynamic size of the nanomaterials. SEM micrographs of the hybrid nanoparticles also confirmed a similar particle size.

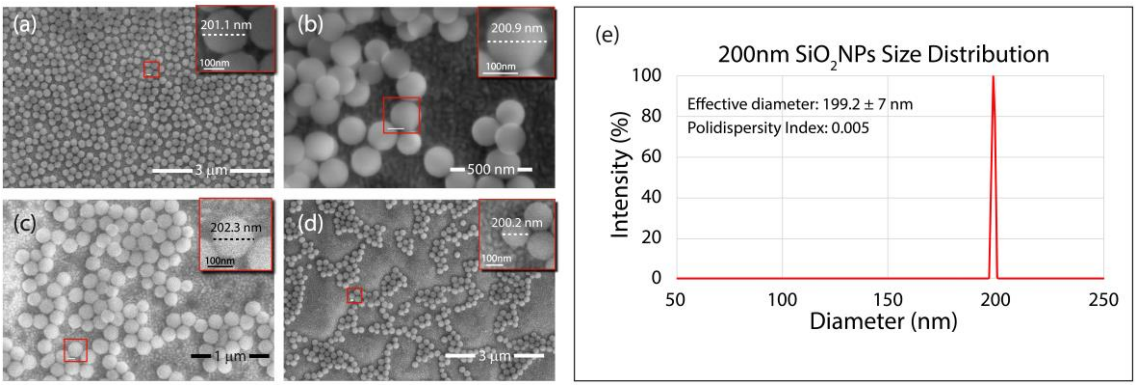

Figure 4. (left) SEM micrographs of the nanoparticles immobilized over Au wafers: (a) Au_SiO_2@APTES; (b) Au_SiO_2@Lys-Lys; (c) Au_SiO_2@(G_2); (d) Au_SiO_2@(G_3)PEG. (right) DLS spectrum of the SiO_2NPs

3.3. Intramolecular interaction

The interaction between CO_2 and both SiO_2NPs and SiO_2@APTES was calculated to obtain a clear picture of the nature of the adsorption. In that regard, the strength of the intramolecular interaction between CO_2 and a fragment representing the two species was calculated using the following formula.

$$E_{int} = E_{complex} - (E_{CO2} + E_{org.ligand}) \qquad (1)$$

The density functional theory (DFT) approximation (Gaussian 09) under Pople's 6-31G+(d,p) basis set was used for the calculations. The zero-point energy (ZPE) of each species was considered to calculate the respective ΔZPE. Additionally, to account for basis-set superposition error (BSSE), counterpoise correction (CPC) [41] was conducted as implemented in Gaussian. Figure S25 shows two representative fragments of the species subjected to the study. The same orientation was studied in both cases, where the CO_2 molecule is located in the Z axis, directly above the nitrogen and the oxygen atoms. In Tables 1 and 2, some geometry and energy parameters of the two complexes are shown. The C-O-C angle for the SiO_2@APTES@CO_2 complex is more distorted (176.4°) than SiO_2@CO_2, which is expected to correspond to the largest value of charge transfer [41].

Table 1. Calculated interaction energies (E_{int}) with the B3LYP functional (kJ/mol) for the in plane under study

B3LYP									
(SiO_2@APTES@CO_2)-complex					**(SiO_2@CO_2)-complex**				
6-31+G**	6-311+G**	NH_2-C_{CO2}	H-O_{CO2}	O-C-O	6-31+G**	6-311+G**	O_{OH}-O_{CO2}	H-O_{CO2}	O-C-O
E_{int}(kJ/mol)	E_{int}(kJ/mol)	2.95[(1)(3)]	3.33[(1)(3)]	176.4[(1)(	E_{int}(kJ/mol)	E_{int}(kJ/mol)	2.91[(1)(3)]	3.02[(1)]	178.2[(1)(3)]
-12.15	-11.29	2.97[(2)]	3.35[(2)(3)]	176.7[(2)(	-9.64	-9.44	2.89[(2)(3)]	3.04[(2)(3)]	178.2[(2)(3)]

[(1)]6-31 g+(d,p), [(2)]6-311 g+(d,p), [(3)]in Angstroms

Table 2. Calculated ESP charges for the two different complexes under study for the selected atoms

Complex	N	O	C
SiO_2@APTES@CO_2	-0.777	-	0.820
SiO_2@CO_2	-	-0.733	0.809

Additionally, to discuss the influence of the electrostatic interactions on the distortion of the C-O-C angle and on the values of E_{int}, Table 2 shows the electrostatic surface potential (ESP) charges calculated on the representative fragments of N for the APTES complex and O for the "pristine" SiO_2 complex. The ESP charge on N is more negative than that on O, and the charge on C is more positive in the first case; consequently, the C-$N_{(complex)}$ distance is the shortest in SiO_2@APTES@CO_2. Additionally, the values of E_{int} for the SiO_2@APTES complex are more negative in agreement with the previous remark. These results confirm the presence of a strong interaction between primary amine groups and CO_2.

3.4 Thermal stability of the nanomaterials

TGA in air was carried out on the different samples: SiO_2, SiO_2@APTES, SiO_2@Lys-Lys, SiO_2@(G_2), and SiO_2@(G_3)PEG. TG and their derivative (DTG) curves are shown in Figure 5. The thermal decomposition of the nanomaterials occurs in two (SiO_2NPs), three (SiO_2@APTES, SiO_2@(G_2), SiO_2@(G_3)PEG) and four stages (SiO_2@Lys-Lys). Overall, the samples showed a similar weight loss for the first range (0-200 °C), (Calcd. 5-9 wt. %), which was attributed to the loss of water (i.e., moisture), and a second stage at 200–600 °C ascribed to the condensation of adjacent silanol groups to give siloxane through the loss of a water molecule, showing maximum weight loss temperatures of T_{max} ~400 °C (SiO_2NPs and peptide) and T_{max} ~500 °C (PAMAM based).[42, 43]

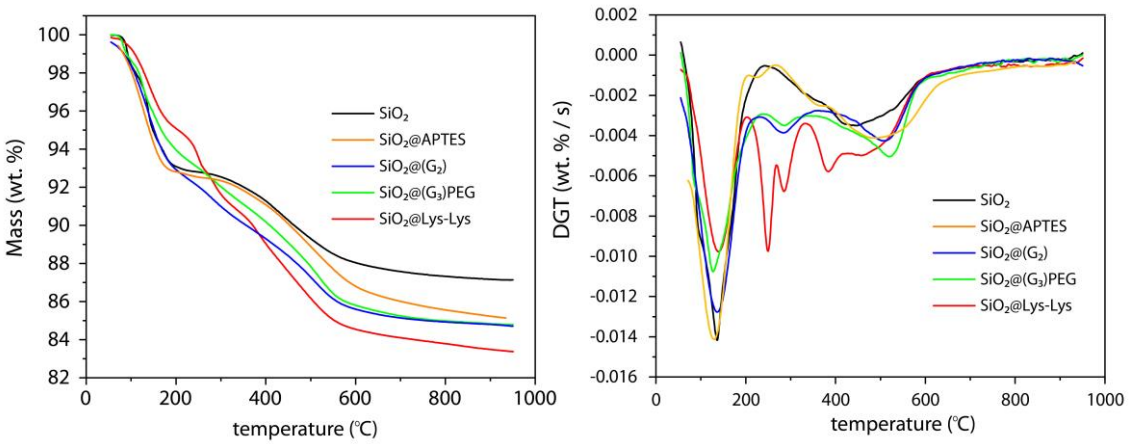

Figure 5. (left) TGA and (right) DTG curves under air flow for pristine (SiO_2Np) and functionalized nanoparticles

At higher temperatures, a very small and constant weight loss (approximately 1 wt. %) was observed up to 950 °C, which can also be due to the condensation of residual silanol

groups [42]. As expected, the functionalized samples displayed additional stages superimposed on the second weight loss stage. Thus, SiO_2@APTES, SiO_2@(G_2), SiO_2@(G_3)PEG and SiO_2@Lys-Lys showed one new short stage at 200-350 °C due to the probable decomposition of dendritic branches and peptide cleavage. Surprisingly, SiO_2@Lys-Lys showed an additional third stage of weight loss (350-420 °C), with a T_{max} of ~385 °C, which might be ascribed to the decomposition of the remaining amino acid branches. It is important to note that since the condensation of silanol groups occurs in a wide range of temperatures (200–600 °C) and the decomposition stages of the dendrites and peptides are superimposed on the latter, it was difficult to identify the nature of each weight loss along this range of temperatures in the functionalized samples. Thus, the recorded total weight loss was 5.1 wt.% for SiO_2NPs, which corresponds to silanol condensation and was 6.1, 7.3, 8.1 and 10.5 wt. % for the SiO_2@APTES, SiO_2@(G_2), SiO_2@(G_3)PEG and SiO_2@Lys-Lys samples, respectively, which corresponds to the silanol condensation and the decomposition of dendrites and peptides.

3.5 Porosity of the SiO_2 nanoparticles

The N_2 adsorption-desorption isotherms for the SiO_2 nanospheres are displayed in Figure 6d. All of them showed type II isotherms typical of nonporous materials [44]. The absence of a hysteresis loop indicates that these materials do not have mesopores.

Table 3. Textural parameters calculated from the N_2 and CO_2 adsorption isotherms at 196 and 0 °C, respectively

	N_2		**CO_2**			
Sample	S_{BET} (m^2/g)	V_T (cm^3/g)	$V_{\mu p}$ (cm^3/g)	Ec (kJ/mol)	Reduction in S_{BET} (%)	Reduction in V_T (%)
SiO_2NPs	19.8	0.034	0.129	22.6	-	
SiO_2@APTES	13.3	0.023	0.102	24.2	33	31
SiO_2@(G_2)	14.3	0.027	0.107	23.2	28	19
SiO_2@(G_3)PEG	14.1	0.026	0.103	22.9	29	23
SiO_2@Lys-Lys	14.4	0.024	0.110	22.6	27	30

The high N_2 adsorption that takes place at relative pressures (P/P°) above 0.98 is due to the condensation of the adsorbate in the inter-nanoparticle space. As can be expected from the shape of the isotherms, these samples displayed low BET surface areas (see Table 3) because of the external surface functionalization of the nanoparticles. SiO_2 nanoparticles have the highest BET surface area, 19.8 m^2/g, which drops to 14 m^2/g after the different functionalization procedures. This decrease is ascribed to the fact that the ligands occupy

part of the surface of the SiO_2NPs, reducing the effective surface area. The total pore volume calculated at 0.95, before the rise at relative pressures close to 1, is only 0.02-0.03 cm^3/g, in agreement with the low N_2 adsorption of these samples. However, they adsorb CO_2 in an appreciable amount (Figure 6a). CO_2 isotherms at 273 K can be classified as type I, despite the low relative achieved, which is typical of microporous materials [44]. From these isotherms, the volume of narrow micropores was calculated [44, 45], with values of 0.129 for the SiO_2 nanoparticles and between 0.102 and 0.124 cm^3/g for the functionalized samples. These values are 100-fold greater than the total pore volume calculated from the N_2 isotherms. This indicates the existence of other additional adsorption centres for CO_2, probably the existence of ultramicropores that are not accessible to N_2 at -196 °C, but they are accessible to CO_2 at 0 °C.

3.6 CO_2 adsorption study

Pristine and functionalized SiO_2 nanoparticles were tested as sorbents for CO_2 capture at temperatures of 0, 25 and 50 °C (Figures 6a-c).

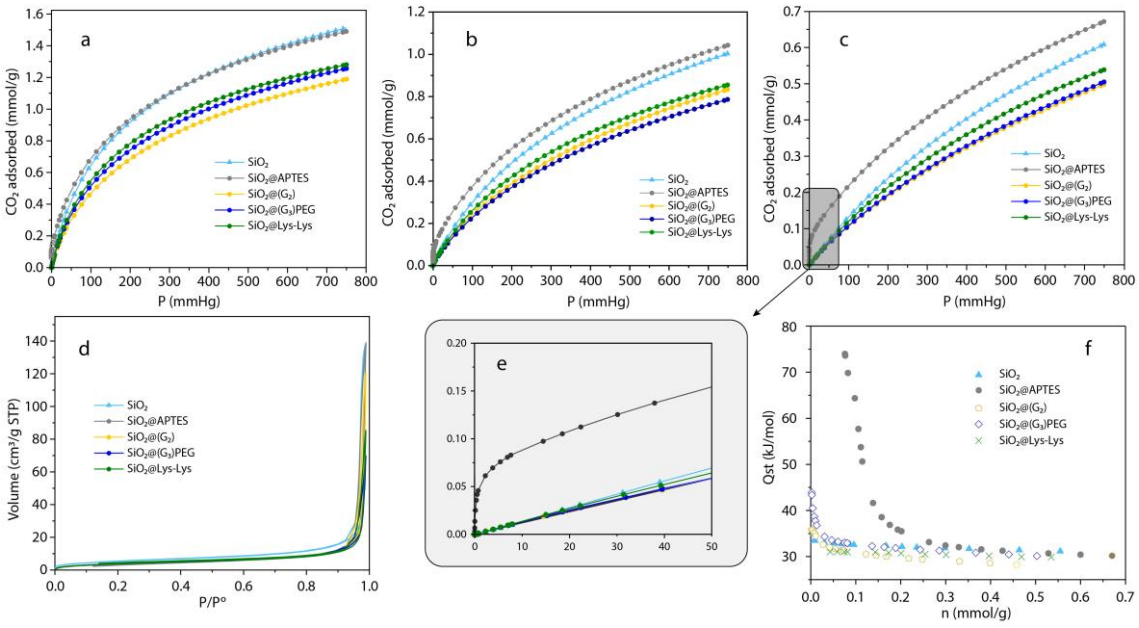

Figure 6. CO_2 adsorption isotherms at (a) 0, (b) 25, and (c) 50 °C for pristine and functionalized nanoparticles. (d) N_2 adsorption-desorption isotherms at -196 °C for the different samples. (e) inset, (f) Isosteric heat of adsorption (Q_{st})

By increasing the temperature, the amount of CO_2 adsorbed decreased according to a physisorption process. The sample coated with APTES (SiO_2@APTES) adsorbs CO_2 more efficiently than pristine SiO_2NPs, particularly at pressures below 200 mmHg (<270

mbars). The decrease in the amount adsorbed with temperature occurs to a lesser extent for the functionalized samples than in pristine SiO_2Np (see Figures S26 – S30), which is related to the existence of adsorption sites with higher adsorption energy in the functionalized samples, as will be seen below. The SiO_2@APTES displayed the highest CO_2 uptakes, despite showing the lowest textural parameters (BET surface area, total pore volume and ultramicropore volume, Table 3). This can be explained by the existence of functional groups that strongly interact with CO_2, thus displaying a marked slope in the range of 0-10 mmHg (Figure 6e). The other three functionalized samples, SiO_2@(G_2), SiO_2@(G_3)PEG, and SiO_2@Lys-Lys, adsorb less CO_2 than the pristine SiO_2NPs, which can be explained by the equilibrium between the porosity and the functional groups being overbalanced and the volume of functional groups not compensating for the decrease in the number of adsorption sites. The behaviour observed in the adsorption of CO_2 at different temperatures can be explained by considering the adsorbent-adsorbate interactions that can be estimated through calculations of the isosteric heat of adsorption, O_{st}. This parameter was obtained by applying the Clausius-Clapeyron equation at several adsorbate coverages (n) from the CO_2 adsorption isotherms at the three temperatures studied here. As shown in Figure 6f, pristine SiO_2Np presented an isosteric heat of adsorption that was almost constant with the degree of surface coverage, falling from 35 kJ/mol at zero coverage to 31 kJ/mol at the highest n. This value at zero coverage is in agreement with the typical values, which are between 30 and 42 kJ/mol reported for zeolites and metal-organic frameworks (MOFs) [6, 46]. Similar Q_{st} values were obtained for the SiO_2@Lys-Lys and SiO_2@(G_2) samples; a value of 44 kJ/mol was recorded for SiO_2@(G_3)PEG, and a fair value of 74 kJ/mol was achieved for SiO_2@APTES. These results are in agreement with the existence of adsorption sites bearing different adsorption energies. For sites where the CO_2 molecules will be adsorbed in the most thermodynamically favourable way at low coverage values and when these energetic sites are covered, the adsorption occurs in the less energetic ones (i.e., the pristine surface of the SiO_2NPs). At maximum coverage (Q_{st}), SiO_2@(G_3)PEG displayed n = 0.05 mmol/g, whereas SiO_2@APTES showed n = 0.2 mmol/g due to the lack of high energetic sites available, consistent with PEGylated anchoring on the surface. The reasonable adsorption capacity of SiO_2@APTES at pressures < 5 mmHg (7 mbar) (see Figure 6e and Figure S31) makes them candidates from the prebiotic point of view, as they could promote the formation of ammonium glycinate upon UV irradiation [47].

In a PCC process, diluted CO_2 (typically its concentration is lower than 15 vol.%) has to be efficiently separated from the other gases, mainly N_2, that form the flue gas streams. Thus, the selectivity of the adsorbent is an important factor in CO_2 capture. Figure 7 shows the predicted selectivity of adsorption of CO_2 over N_2 at 1 bar and at 25 and 50 °C for pristine SiO_2NPs and sample SiO_2@APTES as a function of the CO_2 mole fraction in a stream composed of CO_2 and N_2. The CO_2/N_2 adsorption selectivity decreased with increasing CO_2 mole fraction in the mixture for both samples and at the two temperatures. The functionalized sample showed a higher selectivity than the pristine nanoparticles. For the case of the functionalized sample, the selectivity increased with the adsorption temperature, contrary to what occurred for the nonfunctionalized nanoparticles. This is due to the high adsorption energy that helps the amount of CO_2 adsorbed to remain high as the adsorption temperature increases.

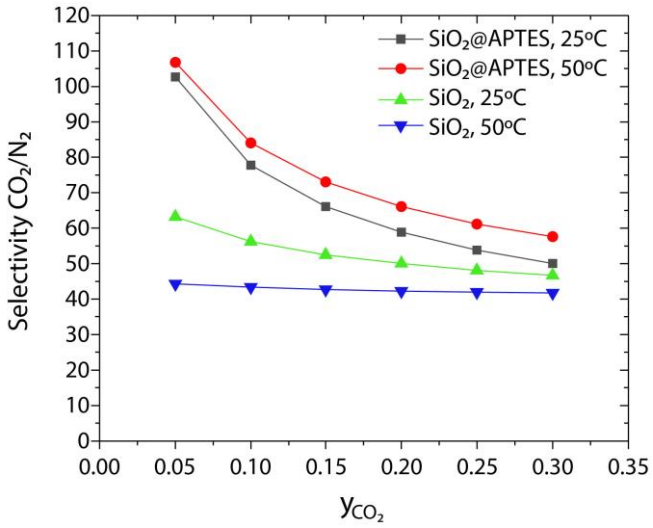

Figure 7. The predicted selectivity of adsorption of CO_2 over N_2 in a mixture of both gases at 1 bar and at 25 and 50 °C as a function of the CO_2 mole fraction on the PPNs

Selectivity depends not only on adsorption temperature and mole fraction but also on pressure; therefore, it is difficult to compare with other materials if the experimental conditions are not similar. However, the functionalized sample achieved very high adsorption selectivity, especially at a low CO_2 mole fraction, compared to other materials previously reported. Thus, at 25 °C, 1 bar and 0.15 CO_2 molar fraction, a CO_2/N_2 selectivity of approximately 10 was reported for non-doped porous carbons [48], which increases at values between 13 and 80 for N-doped carbons [49]. In the case of metal-organic frameworks (MOFs) at 25 °C, 1 bar and 0.1 CO_2 molar fraction, values of approximately 79 have been reported [50]. The high selectivity values of SiO_2@APTES

indicate a stronger ability to separate CO_2/N_2; thus, we can conclude that these materials are potentially interesting for CO_2 separation.

Finally, to verify the regeneration performance and working capacities of SiO_2@APTES, five adsorption and desorption cycles were conducted at 25 °C and 1 bar under exposure to CO_2 (Figure 8). No significant drop in dynamic adsorptive capacity was observed; furthermore, the CO_2 breakthrough in the 5 cycles was constant with variations <2% in the mmol/g adsorbed.

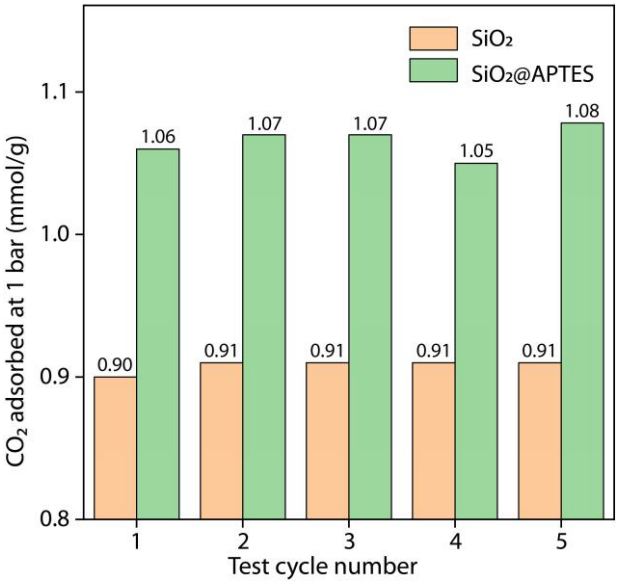

Figure 8. Working capacity of SiO_2@APTES under repeated adsorption cycles at 25 °C and 1 bar

3. CONCLUSIONS

Amine-functionalized (branched and linear) nonmesoporous silica nanoparticles were successfully synthesized, and each step was assessed by both colorimetry and XPS/IR spectroscopy. In the present work, the CO_2 adsorption capacity and isosteric heat of adsorption values were investigated on bare SiO_2NPs and their hybrid counterparts, SiO_2@APTES, SiO_2@(G_2), SiO_2@(G_3)PEG and SiO_2@Lys-Lys, at three different temperatures, and their behaviour at low vacuum CO_2 pressures, mimicking Martian atmospheric conditions, was studied. We showed that, as expected, primary amine groups are a key point in the CO_2 adsorption process, as they are energetically preferred binding sites compared to nanoparticle surface silanols. Indeed, SiO_2@APTES showed a higher affinity towards CO_2 than pristine SiO_2NPs; however, it was surprising to observe the opposite trend for the rest of the hybrid nanoparticles, which might be a consequence of

i) the inherent interaction between the branched ligands and the Si-OH surface itself and ii) the microporous blockage, which was intensified by the presence of bulky groups. The better performance of SiO_2@APTES despite having a similar loss of surface area (30%) compared to the other hybrid nanoparticles demonstrates the important role of the surface absorption characteristics as well as the porosity features in the bare nanomaterial. Further studies should aim to find the optimal conditions for decorating sorbets bearing larger porosity surfaces with such dendritic ligands.

Declaration of competing interests

The authors declare that they have no known competing financial interests or personal relationships that could have appeared to influence the work reported in this paper.

ACKNOWLEDGMENTS

This work has been supported by MINECO grants PID2019-104205GB-C21 and PID2019-107442RB-C32) and has been partially funded by the Spanish State Research Agency (AEI) Project No. MDM-2017-0737 Unidad de Excelencia "María de Maeztu"-Centro de Astrobiología (INTA-CSIC) and by PCTI 2013-2017 from the Principado de Asturias and ERDF through projects RTI2018-100832-B-I00 and IDI/2018/000233. E. C. D: Talent Attraction Postdoctoral Fellowship from CAM, reference: 2018-T2/TIC-10616. The authors also thank Maite Sampedro for her help during IR measurements.

REFERENCES

[1] A. Perejón, L.M. Romeo, Y. Lara, P. Lisbona, A. Martínez, J.M. Valverde, The Calcium-Looping technology for CO2 capture: On the important roles of energy integration and sorbent behavior, Applied Energy 162 (2016) 787-807.
[2] B. Belaissaoui, E. Favre, Membrane Separation Processes for Post-Combustion Carbon Dioxide Capture: State of the Art and Critical Overview, Oil Gas Sci. Technol. – Rev. IFP Energies nouvelles 69(6) (2014) 1005-1020.
[3] A. Hart, N. Gnanendran, Cryogenic CO2 capture in natural gas, Energy Procedia 1(1) (2009) 697-706.
[4] P.J.E. Harlick, F.H. Tezel, Adsorption of carbon dioxide, methane and nitrogen: pure and binary mixture adsorption for ZSM-5 with SiO2/Al2O3 ratio of 280, Separation and Purification Technology 33(2) (2003) 199-210.
[5] H.J. Herzog, Peer Reviewed: What Future for Carbon Capture and Sequestration?, Environmental Science & Technology 35(7) (2001) 148A-153A.
[6] K. Sumida, D.L. Rogow, J.A. Mason, T.M. McDonald, E.D. Bloch, Z.R. Herm, T.-H. Bae, J.R. Long, Carbon Dioxide Capture in Metal–Organic Frameworks, Chemical Reviews 112(2) (2012) 724-781.
[7] I.G.B.N. Makertihartha, P.T. Dharmawijaya, M. Zunita, I.G. Wenten, Post combustion CO2 capture using zeolite membrane, AIP Conference Proceedings 1818(1) (2017) 020074.

[8] E.J. Cueto Díaz, S. Gálvez-Martínez, M.C. Torquemada Vico, M.P. Valles González, E. Mateo-Martí, 2-D organization of silica nanoparticles on gold surfaces: CO2 marker detection and storage, RSC Advances 10(53) (2020) 31758-31764.
[9] L. Michels, J.O. Fossum, Z. Rozynek, H. Hemmen, K. Rustenberg, P.A. Sobas, G.N. Kalantzopoulos, K.D. Knudsen, M. Janek, T.S. Plivelic, G.J. da Silva, Intercalation and Retention of Carbon Dioxide in a Smectite Clay promoted by Interlayer Cations, Scientific Reports 5(1) (2015) 8775.
[10] Á. Sánchez-Sánchez, F. Suárez-García, A. Martínez-Alonso, J.M.D. Tascón, Influence of Porous Texture and Surface Chemistry on the CO2 Adsorption Capacity of Porous Carbons: Acidic and Basic Site Interactions, ACS Applied Materials & Interfaces 6(23) (2014) 21237-21247.
[11] A. Aboudheir, P. Tontiwachwuthikul, A. Chakma, R. Idem, Kinetics of the reactive absorption of carbon dioxide in high CO2-loaded, concentrated aqueous monoethanolamine solutions, Chemical Engineering Science 58(23) (2003) 5195-5210.
[12] P. Luis, Use of monoethanolamine (MEA) for CO2 capture in a global scenario: Consequences and alternatives, Desalination 380 (2016) 93-99.
[13] Y.E. Kim, S.H. Yun, J.H. Choi, S.C. Nam, S.Y. Park, S.K. Jeong, Y.I. Yoon, Comparison of the CO2 Absorption Characteristics of Aqueous Solutions of Diamines: Absorption Capacity, Specific Heat Capacity, and Heat of Absorption, Energy & Fuels 29(4) (2015) 2582-2590.
[14] A. Wilk, L. Więcław-Solny, A. Tatarczuk, A. Krótki, D. Śpiewak, Investigation of effects of the amine solutions composition on carbon dioxide absorption rate and capacity, 2012.
[15] B. Fadhel, M. Hearn, A. Chaffee, CO2 adsorption by PAMAM dendrimers: Significant effect of impregnation into SBA-15, Microporous and Mesoporous Materials 123(1) (2009) 140-149.
[16] R. Sanz, G. Calleja, A. Arencibia, E.S. Sanz-Pérez, CO2 adsorption on branched polyethyleneimine-impregnated mesoporous silica SBA-15, Applied Surface Science 256(17) (2010) 5323-5328.
[17] L. Zhang, N. Zhan, Q. Jin, H. Liu, J. Hu, Impregnation of Polyethylenimine in Mesoporous Multilamellar Silica Vesicles for CO2 Capture: A Kinetic Study, Industrial & Engineering Chemistry Research 55(20) (2016) 5885-5891.
[18] U. Patil, A. Fihri, A.-H. Emwas, V. Polshettiwar, Silicon oxynitrides of KCC-1, SBA-15 and MCM-41 for CO2 capture with excellent stability and regenerability, Chemical Science 3(7) (2012) 2224-2229.
[19] B. Singh, V. Polshettiwar, Design of CO2 sorbents using functionalized fibrous nanosilica (KCC-1): insights into the effect of the silica morphology (KCC-1 vs. MCM-41), Journal of Materials Chemistry A 4(18) (2016) 7005-7019.
[20] J.H. Drese, S. Choi, R.P. Lively, W.J. Koros, D.J. Fauth, M.L. Gray, C.W. Jones, Synthesis–Structure–Property Relationships for Hyperbranched Aminosilica CO2 Adsorbents, Advanced Functional Materials 19(23) (2009) 3821-3832.
[21] J.C. Hicks, J.H. Drese, D.J. Fauth, M.L. Gray, G. Qi, C.W. Jones, Designing Adsorbents for CO2 Capture from Flue Gas-Hyperbranched Aminosilicas Capable of Capturing CO2 Reversibly, Journal of the American Chemical Society 130(10) (2008) 2902-2903.
[22] D.R. Kumar, C. Rosu, A.R. Sujan, M.A. Sakwa-Novak, E.W. Ping, C.W. Jones, Alkyl-Aryl Amine-Rich Molecules for CO2 Removal via Direct Air Capture, ACS Sustainable Chemistry & Engineering 8(29) (2020) 10971-10982.
[23] G. Qi, Y. Wang, L. Estevez, X. Duan, N. Anako, A.-H.A. Park, W. Li, C.W. Jones, E.P. Giannelis, High efficiency nanocomposite sorbents for CO2 capture based on amine-functionalized mesoporous capsules, Energy & Environmental Science 4(2) (2011) 444-452.
[24] J. Xie, N.C. Ellebracht, C.W. Jones, Inter- and Intramolecular Cooperativity Effects in Alkanolamine-Based Acid-Base Heterogeneous Organocatalysts, ACS omega 4(1) (2019) 1110-1117.

[25] D.V. Quang, A. Dindi, M.R.M. Abu-Zahra, One-Step Process Using CO2 for the Preparation of Amino-Functionalized Mesoporous Silica for CO2 Capture Application, ACS Sustainable Chemistry & Engineering 5(4) (2017) 3170-3178.
[26] E. Mateo-Martí, O. Prieto-Ballesteros, J.M. Sobrado, J. Gómez-Elvira, J.A. Martín-Gago, A chamber for studying planetary environments and its applications to astrobiology, Measurement Science and Technology 17(8) (2006) 2274-2280.
[27] J.R. Matthews, D. Tuncel, R.M.J. Jacobs, C.D. Bain, H.L. Anderson, Surfaces Designed for Charge Reversal, Journal of the American Chemical Society 125(21) (2003) 6428-6433.
[28] M. Tajabadi, M.E. Khosroshahi, S. Bonakdar, An efficient method of SPION synthesis coated with third generation PAMAM dendrimer, Colloids and Surfaces A: Physicochemical and Engineering Aspects 431 (2013) 18-26.
[29] A. Chaix, E. Cueto-Diaz, A. Delalande, N. Knezevic, P. Midoux, J.-O. Durand, C. Pichon, F. Cunin, Amino-acid functionalized porous silicon nanoparticles for the delivery of pDNA, RSC Advances 9(55) (2019) 31895-31899.
[30] E. Poli, V. Chaleix, C. Damia, Z. Hjezi, E. Champion, V. Sol, Efficient quantification of primary amine functions grafted onto apatite ceramics by using two UV-Vis spectrophotometric methods, Analytical Methods 6(24) (2014) 9622-9627.
[31] M. V, H.M. Mody, H.C. Bajaj, Effect of Thermal Treatment of Silica Gels on Their Amino Functionalization and Subsequent Adsorption Properties for Cu2+ from Aqueous Solution of Copper Sulfate, Industrial & Engineering Chemistry Research 49(17) (2010) 8184-8191.
[32] S.C. Feifel, F. Lisdat, Silica nanoparticles for the layer-by-layer assembly of fully electro-active cytochrome c multilayers, Journal of Nanobiotechnology 9(1) (2011) 59.
[33] D. Hasan, C. Lee, Hybrid Metamaterial Absorber Platform for Sensing of CO2 Gas at Mid-IR, Advanced Science 5(5) (2018) 1700581.
[34] W. Guan, F. Ji, Q. Chen, P. Yan, L. Pei, Synthesis and Enhanced Phosphate Recovery Property of Porous Calcium Silicate Hydrate Using Polyethyleneglycol as Pore-Generation Agent, Materials 6(7) (2013).
[35] M. Sanchez-Arenillas, S. Galvez-Martinez, E. Mateo-Marti, Sulfur amino acids and alanine on pyrite (100) by X-ray photoemission spectroscopy: Surface or molecular role?, Applied Surface Science 414 (2017) 303-312.
[36] C.-J. Weng, C.-H. Chang, C.-W. Peng, S.-W. Chen, J.-M. Yeh, C.-L. Hsu, Y. Wei, Advanced Anticorrosive Coatings Prepared from the Mimicked Xanthosoma Sagittifolium-leaf-like Electroactive Epoxy with Synergistic Effects of Superhydrophobicity and Redox Catalytic Capability, Chemistry of Materials 23(8) (2011) 2075-2083.
[37] F. Han, S. Yang, W. Jing, K. Jiang, Z. Jiang, H. Liu, L. Li, Surface plasmon enhanced photoluminescence of ZnO nanorods by capping reduced graphene oxide sheets, Optics Express 22(10) (2014) 11436-11445.
[38] A.v. Cresce, S.M. Russell, D.R. Baker, K.J. Gaskell, K. Xu, In Situ and Quantitative Characterization of Solid Electrolyte Interphases, Nano Letters 14(3) (2014) 1405-1412.
[39] C. Shen, G. Hu, L.-Z. Cheong, S. Huang, J.-G. Zhang, D. Wang, Direct Observation of the Growth of Lithium Dendrites on Graphite Anodes by Operando EC-AFM, Small Methods 2(2) (2018) 1700298.
[40] R. Sujith, P.K. Chauhan, J. Gangadhar, A. Maheshwari, Graphene nanoplatelets as nanofillers in mesoporous silicon oxycarbide polymer derived ceramics, Scientific Reports 8(1) (2018) 17633.
[41] E. Hernández-Marín, A.A. Lemus-Santana, Theoretical Study of the Formation of Complexes Between CO2 and Nitrogen Heterocycles, Journal of the Mexican Chemical Society 59 (2015) 36-42.
[42] A.S. Araujo, M. Jaroniec, Thermogravimetric monitoring of the MCM-41 synthesis, Thermochimica Acta 363(1) (2000) 175-180.
[43] H. Landmesser, H. Kosslick, W. Storek, R. Fricke, Interior surface hydroxyl groups in ordered mesoporous silicates, Solid State Ionics 101-103 (1997) 271-277.

[44] M. Thommes, K. Kaneko, A.V. Neimark, J.P. Olivier, F. Rodriguez-Reinoso, J. Rouquerol, K.S.W. Sing, Physisorption of gases, with special reference to the evaluation of surface area and pore size distribution (IUPAC Technical Report), Pure and Applied Chemistry 87(9-10) (2015) 1051-1069.
[45] D. Lozano-Castelló, D. Cazorla-Amorós, A. Linares-Solano, Usefulness of CO2 adsorption at 273 K for the characterization of porous carbons, Carbon 42(7) (2004) 1233-1242.
[46] L. Grajciar, J. Čejka, A. Zukal, C. Otero Areán, G. Turnes Palomino, P. Nachtigall, Controlling the Adsorption Enthalpy of CO2 in Zeolites by Framework Topology and Composition, ChemSusChem 5(10) (2012) 2011-2022.
[47] J.-B. Bossa, F. Borget, F. Duvernay, P. Theulé, T. Chiavassa, How a usual carbamate can become an unusual intermediate: a new chemical pathway to form glycinate in the interstellar medium, Journal of Physical Organic Chemistry 23(4) (2010) 333-339.
[48] J. Park, S.Y. Cho, M. Jung, K. Lee, Y.-C. Nah, N.F. Attia, H. Oh, Efficient synthetic approach for nanoporous adsorbents capable of pre- and post-combustion CO2 capture and selective gas separation, Journal of CO2 Utilization 45 (2021) 101404.
[49] Y. Wang, X. Hu, T. Guo, J. Hao, C. Si, Q. Guo, Efficient CO2 adsorption and mechanism on nitrogen-doped porous carbons, Frontiers of Chemical Science and Engineering 15(3) (2021) 493-504.
[50] Z. Zhang, Y. Zhao, Q. Gong, Z. Li, J. Li, MOFs for CO2 capture and separation from flue gas mixtures: the effect of multifunctional sites on their adsorption capacity and selectivity, Chemical Communications 49(7) (2013) 653-661.